Performance Analysis of Single Receiver Matched-Mode Localization

Yann Le Gall, François-Xavier Socheleau, Julien Bonnel

To cite this version:

Yann Le Gall, François-Xavier Socheleau, Julien Bonnel. Performance Analysis of Single Receiver Matched-Mode Localization. IEEE Journal of Oceanic Engineering, 2019, 10.1109/JOE.2017.2773131 . hal-01772706

HAL Id: hal-01772706
https://hal.science/hal-01772706

Submitted on 20 Apr 2018

HAL is a multi-disciplinary open access archive for the deposit and dissemination of scientific research documents, whether they are published or not. The documents may come from teaching and research institutions in France or abroad, or from public or private research centers.

L'archive ouverte pluridisciplinaire **HAL**, est destinée au dépôt et à la diffusion de documents scientifiques de niveau recherche, publiés ou non, émanant des établissements d'enseignement et de recherche français ou étrangers, des laboratoires publics ou privés.

Performance Analysis of Single Receiver Matched-Mode Localization

Yann Le Gall, Francois-Xavier Socheleau, *Member, IEEE* and Julien Bonnel, *Member, IEEE*

Abstract

Acoustic propagation in shallow water at low frequency is characterized by a few propagating modes. When the source is impulsive or short enough, the modes can be extracted from the signal received on a single sensor using a warping operator. This opens the door to single receiver matched-mode processing (SR-MMP) as a means to estimate source location and/or ocean environmental parameters. While the applicability of SR-MMP has been demonstrated through several experiments, prediction of its achievable performance has not been fully investigated. In this paper, performance analysis of SR-MMP is carried out using numerical simulations of a typical shallow water environment, incorporating possible environmental mismatch as well as degradations resulting from non-ideal modal filtering. SR-MMP is a non-linear estimation problem that presents three regions of operation: the high SNR asymptotic region driven by local errors, the intermediate SNR threshold region driven by sidelobe ambiguities and the low SNR no-information region. The method of interval errors, which gives computationally efficient and reliable mean squared error performance prediction, is used to conduct the analysis. The results suggest that the SR-MMP performance depends strongly on the source/receiver depth. A significant loss in performance is observed when the receiver is located at a node common to two modes. Receiver depth must therefore be chosen with care. SR-MMP seems to be quite robust to mismatch on the seabed properties alone but does not handle well the combined effect of seabed and water column mismatches. Non-ideal modal filtering has a moderate impact on performance.

Index Terms

Underwater acoustics, matched-field processing, matched-mode processing, performance analysis, method of interval errors

Yann Le Gall is with Thales Underwater Systems, Route de Saint Anne du Portzic, Brest, France (e-mail: yann.legallplou@gmail.com). Francois-Xavier Socheleau is with IMT Atlantique, Lab-STICC, UBL, Technopole Brest-Iroise CS83818, Brest 29238, France, France (e-mail: fx.socheleau@imt-atlantique.fr). Julien Bonnel is with the Woods Hole Oceanographic Institution, Woods Hole, MA 02543 USA (e-mail: jbonnel@whoi.edu)

I. INTRODUCTION

Matched-field processing (MFP) has been a topic of great interest for the underwater acoustic community over the past decades [1]. From data collected on an array of sensors, MFP allows the estimation of source position and/or environmental parameters by maximizing a cost function called the *processor* that quantifies the match between the recorded acoustic field and simulated replicas of the acoustic field. At low-frequency in shallow water, the propagation can be described by normal mode theory [2, Ch. 5] and the acoustic field consists of several propagating modes. When the source signal is impulsive or at least short enough, these modes can be extracted from the signal received on a single receiver using a warping operator [3]–[6]. This operation is called single receiver modal filtering. It has recently been extended to (unknown) frequency modulated source signals [7], [8]. Once modes are filtered, whether the source is impulsive or frequency modulated, matched-mode processing (MMP) [9]–[11] can be applied to infer the desired parameter values. When using a single hydrophone, this is referred to as single-receiver MMP (SR-MMP) and is the focus of this paper. SR-MMP is different from classical MMP, which applies in a more general context but requires a vertical array spanning most of the water column to filter the modes [10], [12], [13].

Unlike MFP that considers the total pressure field, MMP explicitly compares the measured modes to simulated mode replicas to estimate the desired parameter values. Working in mode space has the additional advantage of providing physical insight into the estimation scheme which makes it easier to deal with problems such as environmental mismatch [9], [10], [14]. Most modal-based single-receiver inversion algorithms considering transient sources are based on the time-frequency (TF) dispersion of the modes [15]–[17]. These methods allow the estimation of the source/receiver range and some of the seabed geoacoustic properties such as sound speed and density. However, because they are based on the position of the modes in the TF domain (*i.e.* the TF dispersion curves), these methods are only sensitive to the mode phase. They are thus unable to estimate source depth and/or seabed attenuation which are intrinsically related to mode amplitudes. To estimate such parameters, it is required to properly filter the modes and inject their amplitude into the inverse problem. For example, seabed attenuation can be estimated through the study of mode amplitude ratios [18], [19]. Alternatively, SR-MMP takes into account both mode phase and mode amplitude information. If the source signal is perfectly known, it is possible to use the absolute phase and amplitude through a coherent MMP processor. However, this is not possible in a source localization scheme, where the source is inherently unknown. When the source signal is unknown, it is possible to use relative phase and amplitude information through an incoherent modal processor. In the context of source localization, incoherent SR-MMP allows a joint estimation of source depth and range [8], [20]. Only the incoherent case will be considered in the following.

While the applicability of SR-MMP has been demonstrated through several experiments [4], [8], [20]–[23], prediction of its achievable performance remains an open question. SR-MMP performance prediction is, in fact, quite challenging because, like MFP or array MMP methods, SR-MMP attempts to solve a nonlinear inverse problem. Nonlinear parameter estimators are known to exhibit a multimodal structure corresponding to sidelobes on the ambiguity surface that quantifies, in our case, the match between measured and replica modes. Due to these sidelobes, SR-MMP performance is subject to the so-called threshold effect [24]. That is, below a certain level of signal-to-noise ratio (SNR) or a certain sample size called threshold, an abrupt increase of the estimator mean-square error (MSE) is observed. More generally, MSE performance curves for nonlinear estimation typically exhibit three distinct regions as function of the SNR: the "no information" region at very low SNR (driven by ambiguity errors), the asymptotic region at high SNR (driven by mainlobe errors) and the threshold region in between that characterizes the transition from global to local errors [25]. This behavior of MSE is well known [24], but accurate prediction of the performance in the three regions is an open problem in general. A brute-force way to approximate this performance is to resort to Monte-Carlo simulations but this comes at the price of very time-consuming computer simulations. This is particularly true when errors due to sidelobes may rarely occur but may have a significant impact on MSE. An alternative approach to Monte-Carlo simulation is to derive MSE bounds or MSE approximations [26]–[33]. However, not all bounds or MSE approximations are suitable for nonlinear problem performance predictions. The well known Cramer-Rao bound for example is only tight in the high SNR asymptotic region. In this study, the performance of SR-MMP is analyzed through an MSE approximation method called the method of interval errors (MIE). The MIE is designed to yield approximate but reliable error prediction at all SNR regions in a computationally efficient way. The MIE approximation recently derived for MFP performance prediction in [32], [33] under a signal model where the source signal is assumed deterministic unknown is used here for SR-MFP performance analysis. It also allows consideration of realistic situations where the SR matched-mode processors have inaccurate or incomplete information concerning the propagation environment, leading to a mismatch between the actual physical modes and the replicas used to solve the inverse problem.

The paper is organized as follows. The matched-mode processing problem is introduced in a single receiver context in Section II. The MIE approximation for SR-MMP performance prediction is presented in Section III. Finally, numerical examples applied to source localization are presented in Section IV, followed by conclusions in Section V.

Notation: Throughout this paper, lowercase boldface letters denote vectors, e.g., $\mathbf{x}$, and uppercase boldface letters denote matrices, e.g., $\mathbf{A}$. The superscripts ^{T} and ^{H} mean transposition and Hermitian transposition, respectively. The $N \times N$ identity matrix is denoted by $\mathbf{I}_N$. Finally, $\mathbb{E}\{\cdot\}$ denotes expectation, $\mathbb{P}(\cdot)$ denotes the probability measure and δ is the Kronecker delta function.

II. SINGLE RECEIVER CONTEXT

A. Modal propagation and modal filtering

In the studied context, low-frequency sound in shallow water, propagation can be described by normal-mode theory. Considering a broadband source emitting at depth z_s in a range-independent waveguide, the spectral component of the pressure field $y(f)$ received at depth z_r after propagation over a range r_s is given by [2, Ch. 5]:

$$y(f) = s(f) \sum_{m=1}^{M} x_m(f), \tag{1}$$

where $s(f)$ is the source spectrum and M is the number of propagating modes. The quantity $x_m(f)$ is the contribution of mode m to the pressure field. It is expressed as

$$x_m(f) = Q\psi_m(f, z_s)\psi_m(f, z_r)\frac{e^{jr_s k_{rm}(f)}}{\sqrt{k_{rm}(f) r_s}}, \tag{2}$$

where k_{rm} and ψ_m are the horizontal wavenumber and modal depth function of mode m, respectively. The quantity $Q = \frac{e^{j\pi/4}}{\sqrt{8\pi}\rho(z_s)}$ represents a constant factor with $\rho(z_s)$ as the water density at the source depth z_s. For notational convenience, the dependencies in r_s, z_s and z_r are dropped for $x_m(f)$.

To perform MMP, it is necessary to filter the modes. This operation can be done with a single receiver using signal processing transformations known as warping operators [3]. A warping operator transforms a signal $y(t)$ into a new warped signal $\mathbf{W}_h y(t)$ using a warping function $h(t)$:

$$\mathbf{W}_h y(t) = \sqrt{|h'(t)|}\, y[h(t)]. \tag{3}$$

Note that warping is an invertible transformation, and that the inverse warping function is $h^{-1}(t)$. The aim of warping is to linearize the phase of the signal $y(f)$ and it can be adapted to any physical situation by choosing the suitable $h(t)$. Dispersion based warping has been introduced by Le Touzé et al. [4]. Its goal is thus to transform every mode into a single frequency (CW signal). To do so, one suitable warping function is [4], [5], [17]

$$h(t) = \sqrt{t^2 + t_r^2}, \tag{4}$$

with $t_r = r/c_w$ where c_w is an average water sound speed.

It has been demonstrated previously that warping defined in Eq. (4) is a robust transformation which can be applied to most low-frequency shallow-water scenarios without precise knowledge of the environment or the propagation range (t_r can be determined empirically without knowing r_s and c_w) [5], [17]. It is therefore adapted to the context of single receiver MMP and it allows modes to be filtered using the following methodology (illustrated by Fig. 3 in [5])

1) warp the received signal using $h(t)$,
2) go to the TF domain, filter warped mode m, and go back to the time domain,
3) unwarp mode m using $h^{-1}(t)$.

In the next sections, MMP performance will first be studied with and without environmental mismatch assuming that the modes are perfectly filtered. The impact of non-ideal modal filtering on MMP performance will then be illustrated in Sec. IV-F by considering the degradations resulting from this filtering as an additional mismatch.

B. Data model

The goal of SR-MMP is to estimate an unknown parameter set $\boldsymbol{\theta}$ from the modes recorded on a single hydrophone. The parameter set $\boldsymbol{\theta}$ may contain both source position (range, depth), and/or ocean environmental parameters. Consider M modes received on a single receiver. The complex received signal is modeled by the $M \times 1$ vector

$$\mathbf{y}(f_k) = s(f_k) \cdot \mathbf{x}(f_k, \boldsymbol{\theta}) + \mathbf{w}(f_k), \;\; k = 1, ..., K \tag{5}$$

where,

- K is the number of available frequencies f_k.
- $\mathbf{x}(f_k, \boldsymbol{\theta})$ is a complex $M \times 1$ vector representing the contribution of M modes at frequency f_k. The m-th component of $\mathbf{x}(f_k, \boldsymbol{\theta})$ is given by Eq. (2).
- $s(f_k)$ is a deterministic complex scalar representing the source amplitude and phase.
- $\mathbf{w}(f_k)$ is a complex $M \times 1$ vector representing circularly-symmetric, zero mean Gaussian noise that is independent of the source signal. In addition, the noise is assumed to be white across both modes and frequencies, so that

$$\mathbb{E}\left\{\mathbf{w}(f_{k_1})\mathbf{w}^H(f_{k_2})\right\} = \sigma^2_{\mathbf{w}}(f_{k_1})\mathbf{I}_M \delta_{f_{k_1}, f_{k_2}}, \tag{6}$$

  and the noise power $\sigma^2_{\mathbf{w}}(f_k)$ is assumed to be known for each frequency f_k. The assumption of circularly-symmetric uncorrelated Gaussian noise is an approximation. Modal filtering may affect these properties. However, numerical experiments (not shown here) conducted with the modal filters used in Sec. IV-F suggest that for the results presented herein such an assumption is a reasonable approximation.

The set of observations is collected in the following vector

$$\mathbf{y} = [\mathbf{y}^T(f_1),\ \mathbf{y}^T(f_2),\ \dots\ \mathbf{y}^T(f_K)]^T. \tag{7}$$

C. Matched-mode processors

The inverse problem modeled by (5) is commonly solved by maximizing a cost function, known as the matched-mode processor, that quantifies the match between measured and simulated replica modes. A common approach for deriving such processors is to resort the maximum likelihood (ML) framework [34], [35]. ML estimation is known to offer the best asymptotic properties with respect to efficiency and can be applied for any state of source spectral knowledge [35].

Let $p(\mathbf{y}|\boldsymbol{\theta})$ denote the conditional probability density function (pdf) of the observation $\mathbf{y}$ given the source/environmental parameter set $\boldsymbol{\theta}$. According to the observation model of Section II, this pdf satisfies

$$p(\mathbf{y}|\boldsymbol{\theta}) = \frac{1}{\prod_{k=1}^{K} |\pi \sigma_{\mathbf{w}}^2(f_k)|^M} \prod_{k=1}^{K} \exp\left(-\frac{|\mathbf{y}(f_k) - s(f_k)\mathbf{x}(f_k,\boldsymbol{\theta})|^2}{\sigma_{\mathbf{w}}^2(f_k)}\right). \tag{8}$$

The maximum likelihood estimate of the desired parameter set $\boldsymbol{\theta}$ is obtained by maximizing (8) with respect to $\boldsymbol{\theta}$, considering the source signal $s(f_k)$ as a nuisance parameter that is replaced by its ML estimate according to the profile likelihood technique [36].

In the case where no information is available on the sequence $s(f_k)$ and in the absence of mismatch between the actual modes and the simulated replicas, the ML estimate of the desired parameter set $\boldsymbol{\theta}$ is [35]

$$\hat{\boldsymbol{\theta}} = \arg\max_{\boldsymbol{\theta}} C(\boldsymbol{\theta}),\ \text{ with } C(\boldsymbol{\theta}) = \sum_{k=1}^{K} \frac{|\bar{\mathbf{x}}^H(f_k,\boldsymbol{\theta})\mathbf{y}(f_k)|^2}{\sigma_{\mathbf{w}}^2(f_k)}, \tag{9}$$

where $\bar{\mathbf{x}}(f_k,\boldsymbol{\theta})$ is a normalized version of $\mathbf{x}(f_k,\boldsymbol{\theta})$ defined as $\bar{\mathbf{x}}(f_k,\boldsymbol{\theta}) = \frac{\mathbf{x}(f_k,\boldsymbol{\theta})}{\|\mathbf{x}(f_k,\boldsymbol{\theta})\|}$. This MMP is referred to as incoherent because the multiple frequencies are summed incoherently, i.e., with the absolute value that cancels phase information inside the double sum.

In practice, when solving the inverse problem (9), MMP methods may have inaccurate or incomplete information about the oceanic waveguide and the modes may be imperfectly filtered. Consequently, there may be a mismatch between the actual extracted modes and the replicas produced by a numerical model. The sensitivity to environmental mismatch or non-ideal mode filtering can be of particular concern for MMP and a quantitative assessment of its effect on performances is of prime importance. Formally, in presence of mismatch, the assumed modes $\mathbf{x}_\epsilon(f_k, \boldsymbol{\theta})$ used to estimate $\boldsymbol{\theta}$ differ from the extracted modes $\mathbf{x}(f_k, \boldsymbol{\theta})$ and the cost function used in (9) is then expressed as

$$C(\boldsymbol{\theta}) = \sum_{k=1}^{K} \frac{|\bar{\mathbf{x}}_\epsilon^H(f_k, \boldsymbol{\theta})\mathbf{y}(f_k)|^2}{\sigma_{\mathbf{w}}^2(f_k)}, \tag{10}$$

where $\bar{\mathbf{x}}_\epsilon(f_k, \boldsymbol{\theta}) = \frac{\mathbf{x}_\epsilon(f_k,\boldsymbol{\theta})}{\|\mathbf{x}_\epsilon(f_k,\boldsymbol{\theta})\|}$.

III. METHOD OF INTERVAL ERRORS

The MSE of nonlinear estimators is explicitly connected to the shape of the ambiguity function (AF) which quantifies the match between measured and replica modes. Formally, if the true set of parameters is denoted as $\boldsymbol{\theta}_0$, the AF corresponds to the function $C(\boldsymbol{\theta})$ with a noise-free observation and is expressed as:

$$\psi(\boldsymbol{\theta}) = \sum_{k=1}^{K} \gamma(f_k)|\bar{\mathbf{x}}_\epsilon(f_k, \boldsymbol{\theta})^H \bar{\mathbf{x}}(f_k, \boldsymbol{\theta}_0)|^2, \tag{11}$$

where $\gamma(f_k) = \frac{|s(f_k)|^2}{\sigma_{\mathbf{w}}^2(f_k)}\|\mathbf{x}(f_k, \boldsymbol{\theta}_0)\|^2$. For non-linear estimation problems, the ambiguity function exhibits a mainlobe/sidelobe behavior and the MSE presents three regions of operation as a function of SNR: the high SNR asymptotic region driven by mainlobe errors, the intermediate SNR threshold region where there is a strong increase in MSE due to sidelobe errors (also called outliers) and the low SNR no-information region (see Figure 1).

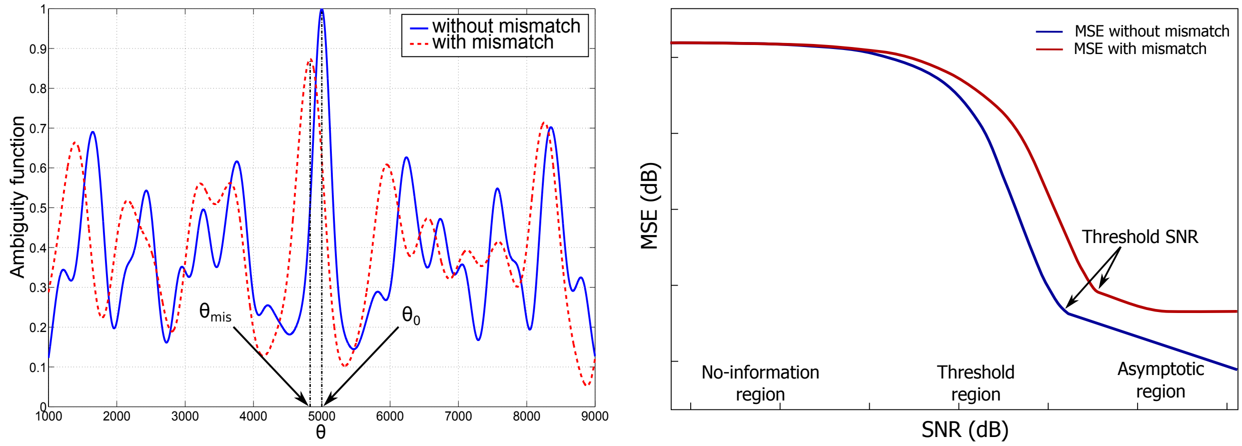

(a) (b)

Fig. 1. Schematic illustration of: (a) the ambiguity function (11) at infinite SNR and (b) MSE regions of a non-linear estimator. (a) is obtained by setting $\gamma(f_k)$ to a constant value, for all k, such that $\psi(\boldsymbol{\theta}_0) = 1$ in the absence of mismatch. When there is no mismatch and no measurement error, the maximum of the ambiguity function is at the true parameter set $\boldsymbol{\theta}_0$. When there is mismatch the estimator can be biased at infinite SNR and the maximum of the ambiguity function is at a value $\boldsymbol{\theta}_{mis} \neq \boldsymbol{\theta}_0$.

MIE provides accurate MSE prediction of nonlinear estimators (see the tutorial treatment by Van Trees and Bell in [37]). MIE builds upon the decomposition of the MSE into two terms: the local errors that concentrate around the mainlobe peak and outliers that concentrate around the sidelobe peaks. Consider the true parameter $\boldsymbol{\theta}_0$ and a discrete set of N_o parameter points $\{\boldsymbol{\theta}_1, \boldsymbol{\theta}_2 \ \ldots \ \boldsymbol{\theta}_{N_o}\}$ sampled at the sidelobe maxima of the AF. The conditional MSE of the ML estimator can then be approximated as [25], [30], [38]–[40]:

$$\mathbb{E}_{\mathbf{y}}\left\{(\hat{\boldsymbol{\theta}} - \boldsymbol{\theta}_0)(\hat{\boldsymbol{\theta}} - \boldsymbol{\theta}_0)^T\right\} \approx \left(1 - \sum_{n=1}^{N_o} P_e(\boldsymbol{\theta}_n|\boldsymbol{\theta}_{\mathrm{m}})\right) \times \mathrm{MSE}^{(\mathrm{asymp})}(\boldsymbol{\theta}_0) + \sum_{n=1}^{N_o} P_e(\boldsymbol{\theta}_n|\boldsymbol{\theta}_{\mathrm{m}}) \times (\boldsymbol{\theta}_n - \boldsymbol{\theta}_0)(\boldsymbol{\theta}_n - \boldsymbol{\theta}_0)^T, \quad (12)$$

where $\boldsymbol{\theta}_{\mathrm{m}}$ denotes the parameter set that maximizes the AF (see Figure 1, when there is no mismatch $\boldsymbol{\theta}_{\mathrm{m}} = \boldsymbol{\theta}_0$ and when there is mismatch $\boldsymbol{\theta}_{\mathrm{m}} = \boldsymbol{\theta}_{mis}$). $P_e(\boldsymbol{\theta}_n|\boldsymbol{\theta}_{\mathrm{m}})$ is the pairwise error probability of the ML estimator (9) possibly under model mismatch (10), i.e. the probability of deciding in favor of the parameter $\boldsymbol{\theta}_n$ in the binary hypothesis test $\{\boldsymbol{\theta}_n, \boldsymbol{\theta}_{\mathrm{m}}\}$.

The pairwise error probability $P_e(\boldsymbol{\theta}_n|\boldsymbol{\theta}_{\mathrm{m}})$ is used as an approximation of the probability that the estimate falls on the sidelobe n and $(1 - \sum_{n=1}^{N_o} P_e(\boldsymbol{\theta}_n|\boldsymbol{\theta}_{\mathrm{m}}))$ is used as an approximation of the probability that the estimate falls on the mainlobe (i.e. the probability of local errors). $\mathrm{MSE}^{(\mathrm{asymp})}(\boldsymbol{\theta}_0)$ is the asymptotic MSE of the ML estimator. In the absence of mismatch, the CRB is usually a good predictor of the performance in this region [32]. Since mismatch is possible, these local errors must be approximated by other means. Analytic expressions for $P_e(\boldsymbol{\theta}_n|\boldsymbol{\theta}_{\mathrm{m}})$ and $\mathrm{MSE}^{(\mathrm{asymp})}(\boldsymbol{\theta}_0)$ have recently been derived [33]. The analytic expressions of $P_e(\boldsymbol{\theta}_n|\boldsymbol{\theta}_{\mathrm{m}})$ and $\mathrm{MSE}^{(\mathrm{asymp})}(\boldsymbol{\theta}_0)$ are summarized in Appendices A and B.

IV. PERFORMANCE ANALYSIS

In this section, the performance of SR-MMP source localization is analyzed in a conventional application framework using MIE. The accuracy of SR-MMP is first studied in the absence of model mismatch for several source and receiver positions. Next, the impact of mismatch between the assumed and the true environments is examined. Finally, the impact of mode filtering on the performance is evaluated. The performance metrics used for the analysis are:

- The MSE in decibel: $(\mathrm{MSE})_{\mathrm{dB}} = 10\log_{10}\left(\mathbb{E}\left\{|\hat{\theta} - \theta_0|^2\right\}\right)$.
- The root mean square error: $\mathrm{RMSE} = \sqrt{\mathbb{E}\left\{|\hat{\theta} - \theta_0|^2\right\}}$.
- The threshold SNR (formally defined in Sec. IV-D).

Depending upon the context, $\hat{\theta}$ (resp. θ_0) either refers to the estimated (resp. true) value of r_s or z_s. In all the studied scenarios, both the source range and depth are assumed unknown.

A. Scenarios

The simulation scenarios considered here are illustrated in Fig. 2. The true environment is made of a water column of height $D = 79$ m, a sound speed profile with a thermocline and a seabed with two sediment layers over a bottom halfspace. The geoacoustic properties of the seabed are shown in Fig. 2 and the values of the sound speed profile are listed in Table I. We consider $K = 50$ frequencies uniformly spaced in the bandwidth $\Delta f = [25, 150]$ Hz and $M = 4$ propagating modes. The SNR is defined as $\mathrm{SNR}(f_k) = \frac{|s(f_k)|^2 \|\mathbf{x}(f_k,\boldsymbol{\theta}_0)\|^2}{\sigma^2_{\mathbf{w}}(f_k)}$ and is constant across frequencies. The search interval for the source position is set (in meters) to $(r_s, z_s) \in [500, 10000] \times [5, 75]$.

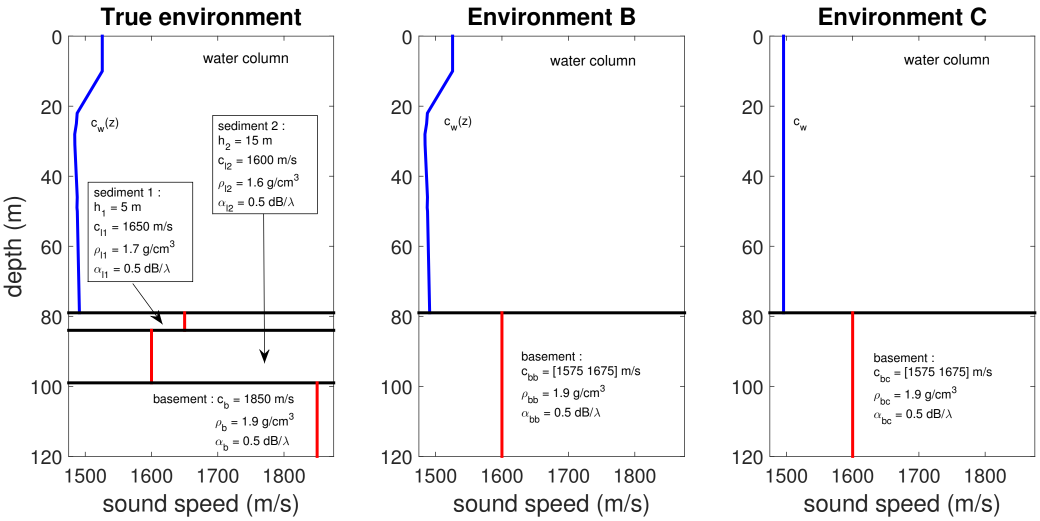

Fig. 2. True environment and and mismatched environments.

In practice, the actual propagation medium is not known perfectly. The detailed structure of the seabed as well as its properties cannot be guessed accurately a priori if geoacoustic inversion campaigns have not been conducted in advance. The sound speed profile is easier to measure (using CTD sensors for instance) but its values may not always be available. Localization is then performed on the basis of an assumed environment that is different from the real one. To assess the impact of such mismatch, two environments are introduced: the B and C environments described in Fig. 2. Environment B is representative of a significant lack of knowledge of the bottom properties. The sound speed profile in the water column is the same as the true one but the seabed is simply made of a bottom halfspace with a constant sound speed c_{bb}. Several values of c_{bb} between 1575 and 1675 m/s will be tested. Environment C is representative of a significant lack of knowledge of the sound speed profile in the water column as well as in the seabed. The sound speed profile in the water column is mistakenly assumed constant at $c_w = 1494.9$ m/s and the seabed is identical to environment B. Several seabed sound speed values between $c_{bc} = 1575$ m/s and $c_{bc} = 1675$ m/s will also be tested.

Depth z (m)	0	10	22	25	28	31	46	49	50	D
Sound speed $c_w(z)$ (m/s)	1525.7	1525.7	1487.8	1486.6	1484.1	1484.3	1487.9	1487.5	1488.0	1491.2

TABLE I

SOUND SPEED PROFILE IN THE WATER COLUMNS FOR THE TRUE ENVIRONMENT AND FOR ENVIRONMENT B.

B. Problem analysis

Fig. 3 shows some examples of AF in the absence of model mismatch. It can be seen that source localization is a multimodal problem so that MIE is well adapted to this context.

The expression of a single mode, as given by (2), allows us to understand the SR-MMP localization problem. Although the estimation of range and depth by MMP is a coupled problem, it should be noted that the information on the depth of the source is carried by the modal function $\psi_m(f, z_s)$ while the range information is mainly carried by the phase term $e^{jr_s k_{rm}(f)}$. Fig. 4 shows the modal depth functions at 100 Hz of the four filtered modes used to perform the SR-MMP localization. Some useful comments:

- The modal depth functions converge to a common node at the surface.
- The modal depth functions present some symmetry with respect to the center of the water column (or antisymmetry depending on the modes parity) slightly distorted by the penetration in the bottom and by the sound speed profile in the water column.
- The amplitudes of the modal depth functions of modes $n = 2$ and $n = 4$ cancel around the depth $z = 45$ m.
- The four modes significantly penetrate into the sediment layers but not much into the basement.

These observations will ease the interpretation of some results obtained in the next sections. For instance, the symmetry of modal functions already explains the shape of the AF in Fig. 3: an approximate axial symmetry is observed with respect to the central depth of the water column.

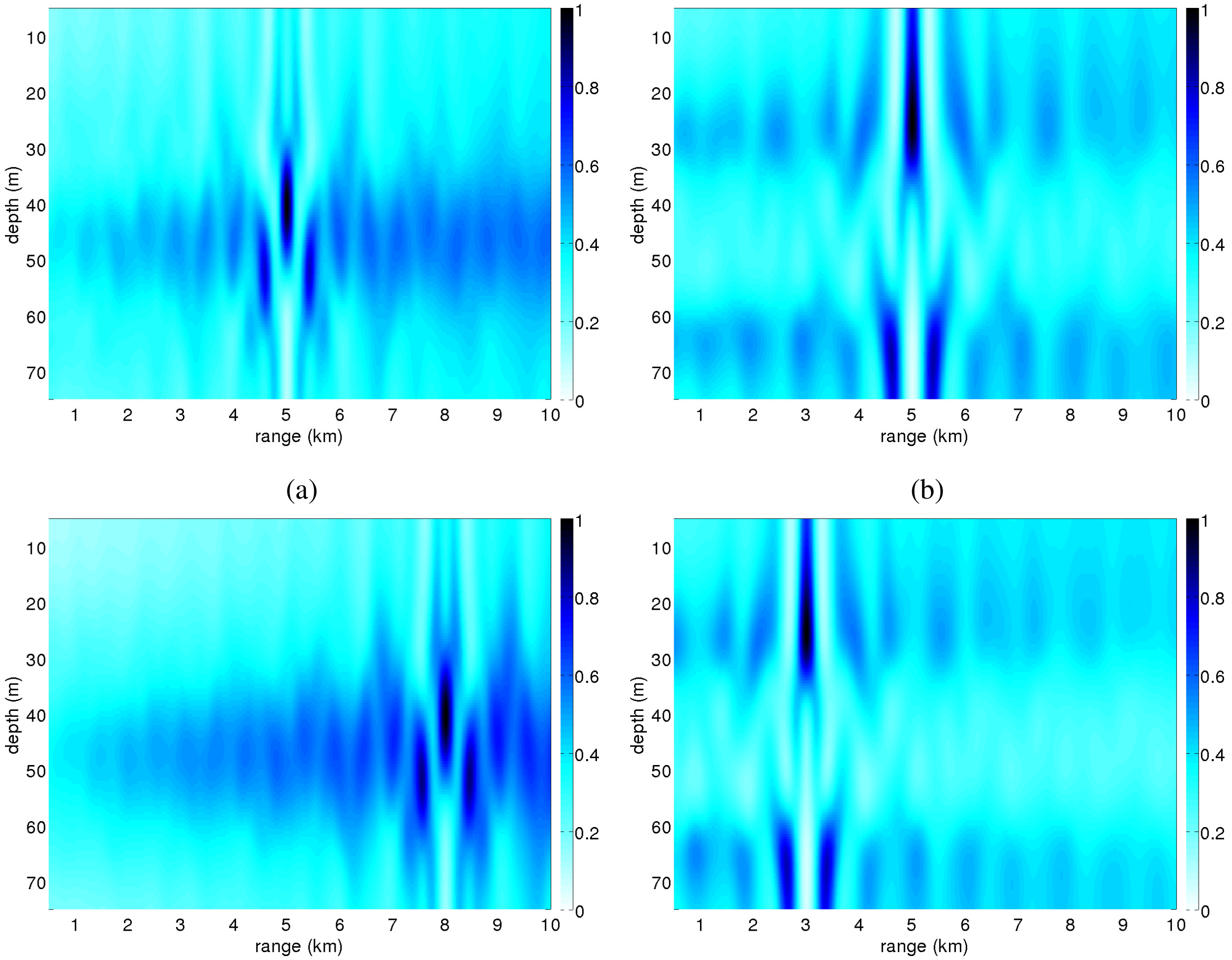

(a) (b)

(c) (d)

Fig. 3. Examples of ambiguity functions of SR-MMP, (a) at $r_s = 5000$ m and $z_s = 40$ m, (b) at $r_s = 5000$ m and $z_s = 25$ m, (c) at $r_s = 8000$ m and $z_s = 40$ m, (d) at $r_s = 3000$ m and $z_s = 25$ m, (in all cases $z_r = 20$ m).

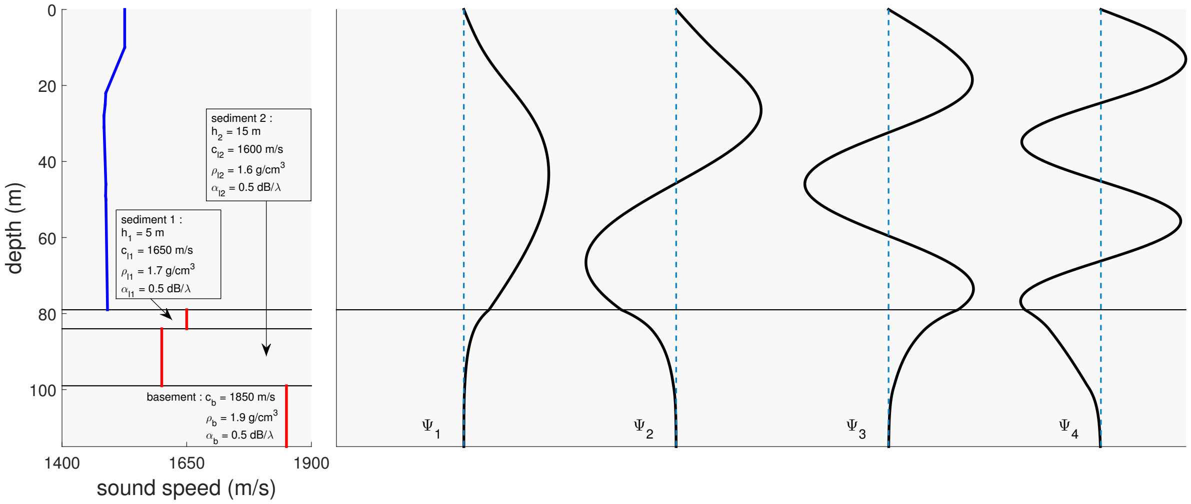

Fig. 4. Modal depths function of the true environment at 100 Hz (only the first four modes are represented).

C. Validation of MIE on a single point

The MIE approach is here validated by comparing its performance predictions with the results obtained by Monte Carlo simulations. The simulations are performed for a single source position: $r_s = 5000$ m and $z_s = 40$ m. Two cases are studied, a first case without mismatch and a case in presence of mismatch. To show the accuracy of MIE, even when the asymptotic MSE is not dominated by the bias $\boldsymbol{\theta}_{\mathrm{m}} - \boldsymbol{\theta}_0$, we here consider a slight mismatch where the assumed values for c_{l1} and c_{l2} in Fig. 2 are 1620 m/s and 1570 m/s, respectively (instead of the true values $c_{l1} = 1650$ m/s and $c_{l2} = 1600$ m/s). Monte Carlo simulations are run over $N_c = 1000$ iterations for each SNR. The choice of the parameter N_o, defined in Sec. III, is based on the shape of the AF. It is set to $N_o = 20$ for all the simulations.

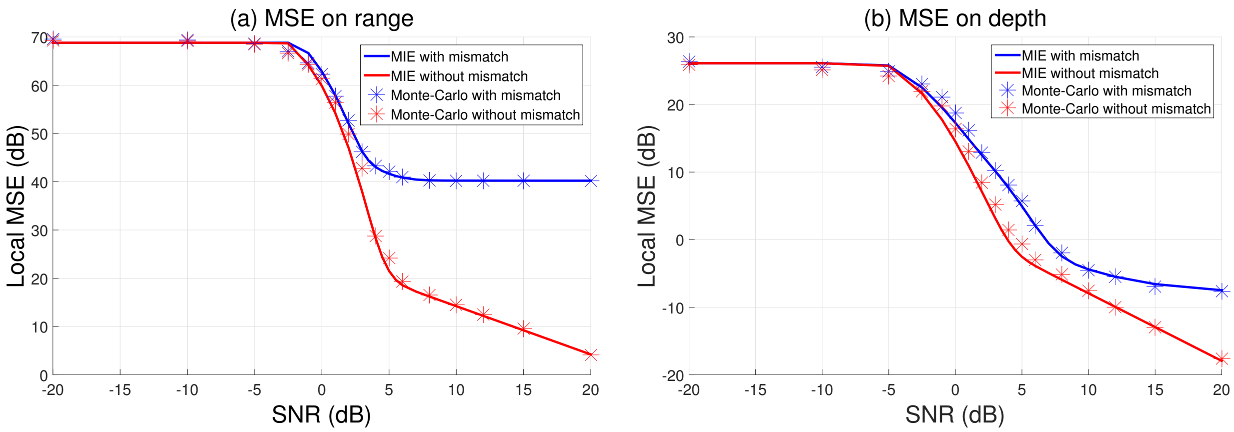

Fig. 5. MIE and Monte-Carlo simulations at $r_s = 5000$ m and $z_s = 40$ m with and without model mismatch.

In both scenarios, a good match between Monte-Carlo simulations and MIE predictions is observed, which validates the use of MIE for this problem. Note that it took a couple of days to get the results of Monte Carlo simulations using Matlab with a contemporary work station (3 GHz CPU with 8 Gb of RAM), whereas MIE provided its results only after a few seconds. Monte Carlo simulations are computationally demanding because they require a large number of realizations and also because the search grid in (r_s, z_s) must be very tight at high SNR to get accurate MSE estimations. In the next sections, the simulations are carried for several environments and a large number of source positions. Therefore, a Monte Carlo approach cannot be used to conduct the analysis (even though the speed could be increased by running the simulations on a parallel cluster or using Fortran/C++ instead of Matlab, it may take days/weeks to obtain the desired results); hence the interest of MIE. In the following, the performance is assessed using MIE only.

D. Performance without environmental mismatch

Performance is first evaluated without environmental mismatch, i.e. both data and replica are simulated in the same environment (A). The MIE is computed over the following search space:

- $r_s \in [500, 10000]$ m with 500 m steps,
- $z_s \in [5, 75]$ m with 4 m steps.

Overall, the MIE is evaluated using $N_l \approx 300$ source positions.

In Fig. 6, the MIE analysis is averaged over the N_l positions so that the MSE can be evaluated for several SNRs. Several receiver depths z_r are also considered. For $z_r = 20$ m and $z_r = 70$ m, performances are nearly equivalent. In both cases, the threshold SNR is around 6 dB and the MSEs are similar. However, the performance decreases for $z_r = 43$ m. The threshold SNR is around 15 dB and the MSE is higher both in the asymptotic region and in the threshold region. As stated in IV-B, the depth functions of modes 2 and 4 have a node at about $z_r = 43$ m (see Fig. 4). Because of this phenomenon, only modes 1 and 3 carry information that can be used by the SR-MMP receiver, which explains the relatively poor performance. In general, if the receiver depth $z_r \notin [40, 50]$ m, then the SR-MMP performances are similar to the ones obtained for $z_r = 20$ m or $z_r = 70$ m. This illustrates the importance of the receiver depth for SR-MMP. In general, we recommend avoiding modal nodes. In the following, the receiver depth is set to $z_r = 20$ m.

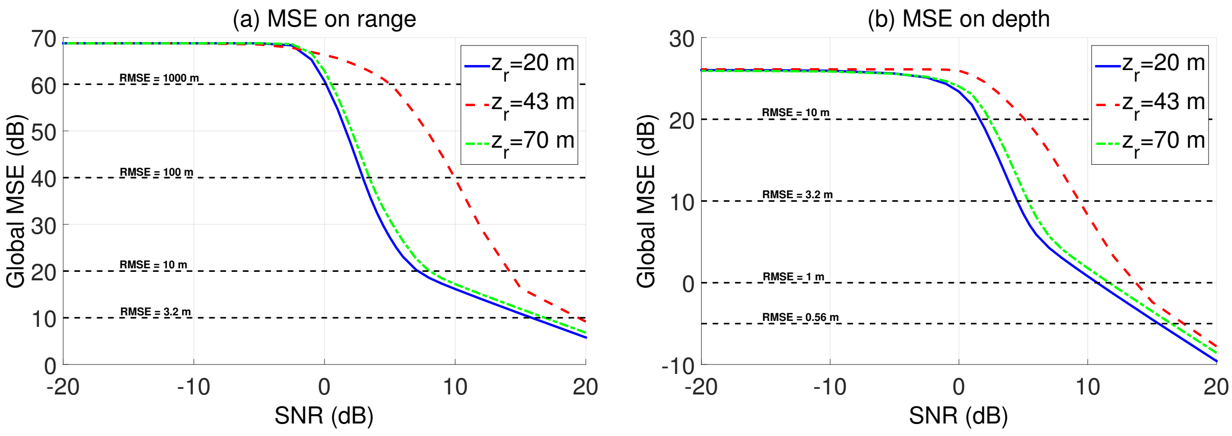

Fig. 6. SR-MMP performance for $r_s \in [500, 10000]$ m and $z_s \in [5, 75]$ m for several receiver depths z_r.

The global MSE (as presented in Fig. 6) reflects the average SR-MMP performance over the search space ($N_l \approx 300$ source positions). However, performance may vary depending on the source position. To quantify this, the performance can be assessed for each source position. Fig. 7 presents several performance metrics in the (z_s, r_s) domain. In particular, this figure shows the threshold SNR, the MSE in the threshold region and the MSE in the asymptotic region. We define the threshold SNR as the lowest SNR satisfying $\sum_{n=1}^{N_o} P_e(\boldsymbol{\theta}_n|\boldsymbol{\theta}_0) > 10^{-4}$. Note that this definition will be used throughout the rest of the paper. In other words, our threshold SNR is the minimal SNR for which the estimate has a probability greater than 10^{-4} to be outside of the AF main lobe. The 10^{-4} value has been chosen empirically by comparing $\sum_{n=1}^{N_o} P_e(\boldsymbol{\theta}_n|\boldsymbol{\theta}_0)$ with the shape of the MSE versus SNR.

The threshold SNR quantifies the SNR below which the performance significantly decreases. However, it does not quantify the performance deterioration. For a given SNR threshold, the error depends on the distance (in range and in depth) between the mainlobe and the sidelobes. We then evaluate the MSE for SNR=4 dB to study the performance in the threshold region. We also evaluate the MSE for SNR=20 dB to evaluate the performance in the asymptotic region. As expected and as illustrated in Fig. 7, these metrics depend on the source position.

First of all, the SNR threshold increases slightly when range r_s increases. There are also particular depths z_s for which the SNR threshold is more important. These areas roughly correspond to modal depth function nodes. In the threshold region (SNR=4 dB), the range MSE reflects the SNR threshold variations, but the depth MSE behavior is more complicated. The depth MSE increases slowly with increasing r_s but the variations with z_s differ. The error increases drastically when the source is not around the middle of the water column. The approximate symmetry of the modal depth functions introduces an approximately symmetric ambiguity increasing as z_s moves closer to the interfaces (surface or seabed).

In the asymptotic region (SNR=20 dB), the range MSE also increases with r_s and is high for particular z_s values (once again corresponding to modal depth function nodes). The depth MSE barely increases with r_s, but depends strongly on z_s. It increases when the source is near the waveguide interfaces and particularly when the source is near the sea surface. These high MSE values are due to the modal behavior in these regions. Indeed, at such depths, the mode amplitude ratios change slowly so that source depth estimation is difficult.

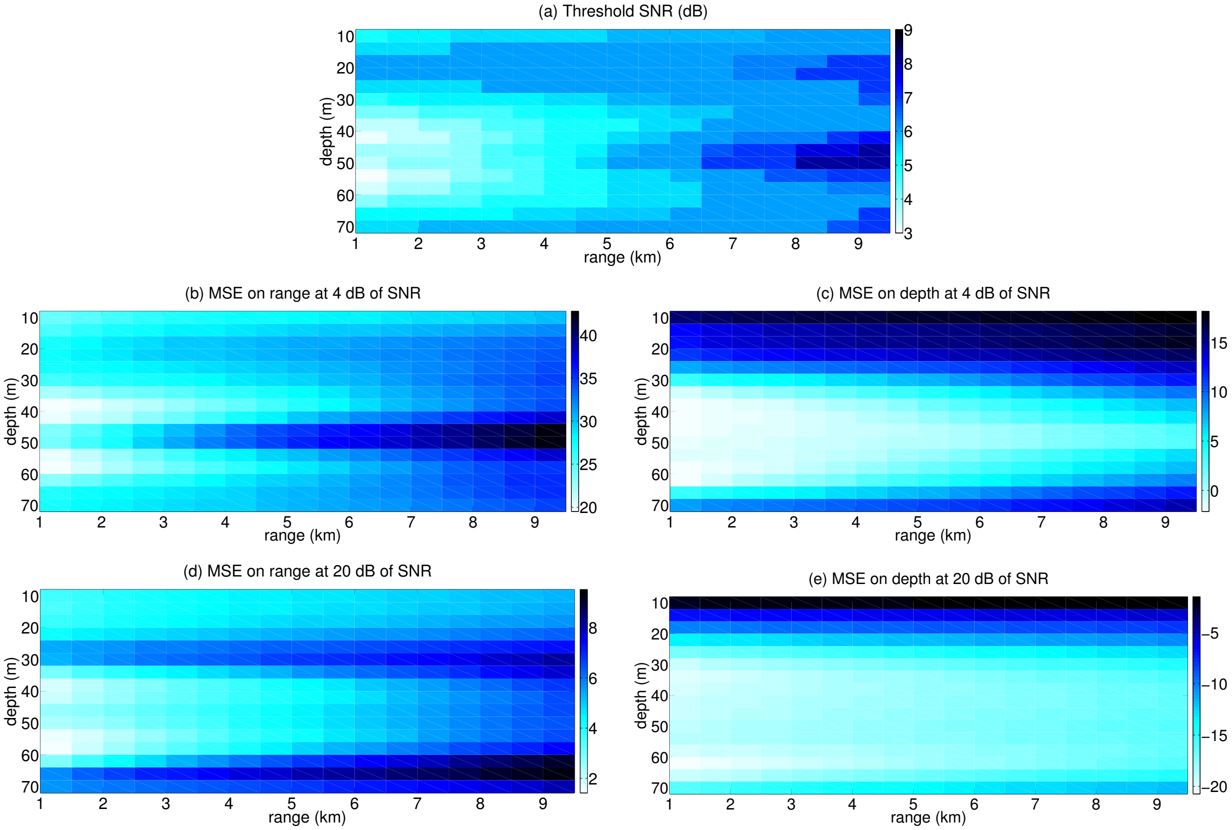

Fig. 7. (a) Threshold SNR, (b) range MSE with SNR=4 dB, (c) depth MSE with SNR=4 dB, (d) range MSE with SNR=20 dB and (e) depth MSE with SNR=20 dB. Every pannel is computed over the search space $r_s \in [500, 10000]$ m and $z_s \in [5, 75]$ m. Receiver depth is $z_r = 20$ m.

E. *Performance with environmental mismatch*

The mismatch impact is evaluated for the two cases presented in Sec. IV-A. We first present the performance when inversion is performed using environment B and then the performance when inversion is performed using environment C. In both cases, data are simulated in environment A and the MIE is computed over the following search space:

- $r_s \in [500, 10000]$ m with 500 m steps,
- $z_s \in [5, 75]$ m with 4 m steps.

Overall, the MIE is evaluated using $N_l \approx 300$ source positions.

1) Inversion using environment B: As stated previously, environment B is representative of a significant lack of knowledge of the seabed properties. Fig. 8 shows the global MSE for several seabed sound speed values c_{bb} (in environment B). For high SNRs, the MSE is obviously higher with seabed mismatch than without, and the performances depend on the c_{bb} value. The best performance is obtained for $c_{bb} = 1625$ m/s. This is expected as the modes are mainly affected by the first two sediment layers in which $c_{l1} = 1600$ m/s and $c_{l2} = 1650$ m/s. Choosing $c_{bb} = 1625$ m/s averages the speed of the first two sediment layers and allows for a reasonably accurate approximation of the propagation (in our frequency band). Except for the case $c_{bb} = 1575$ m/s, the performance deterioration seems relatively minor: for SNR greater than 7.5 dB, the RMSE in range is smaller than 316 m (MSE=50 dB) and smaller than 5.6 m in depth (MSE=15 dB), which is acceptable for most MMP source localization applications. The threshold SNR remains around 6 dB and the MSE increase below this threshold approximately follows the same rate as in the no-mismatch case.

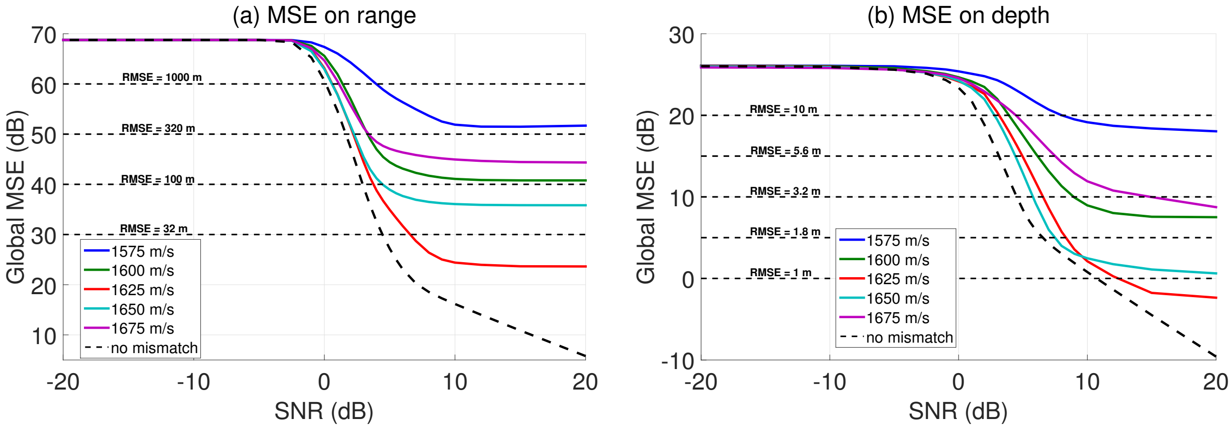

Fig. 8. Inversion using environment B. Global MSE over $r_s \in [500, 10000]$ m and $z_s \in [5, 75]$ m for several seabed sound speeds c_{bb}. Receiver depth is $z_r = 20$ m.

Fig. 9 shows the SNR threshold, the range MSE at 20 dB and the depth MSE at 20 dB in the (z_s, r_s) domain for a seabed speed $c_{bb} = 1625$ m/s. Fig. 10 shows the same performance metrics but for $c_{bb} = 1675$ m/s. Comparing these figures with Fig. 7 nicely illustrates the mismatch impact and the corresponding performance deteriorations.

In the case with mismatch, the MSE global trend is the same as in the case without mismatch. However, several differences exist. Indeed, when considering mismatch, the MSE depends on the modes computed in the true environment (A) and in the assumed environment (B). One should also note that different seabed speeds lead to different performances. As an example, for $c_{bb} = 1625$ m/s the worse performance is found around $z_s = 20$ m while it is found around $z_s = 50$ m for $c_{bb} = 1675$ m/s. Moreover, even if $c_{bb} = 1625$ m/s leads to the best average performance, there are source/SNR configurations where the performance is better with $c_{bb} \neq 1625$ m/s.

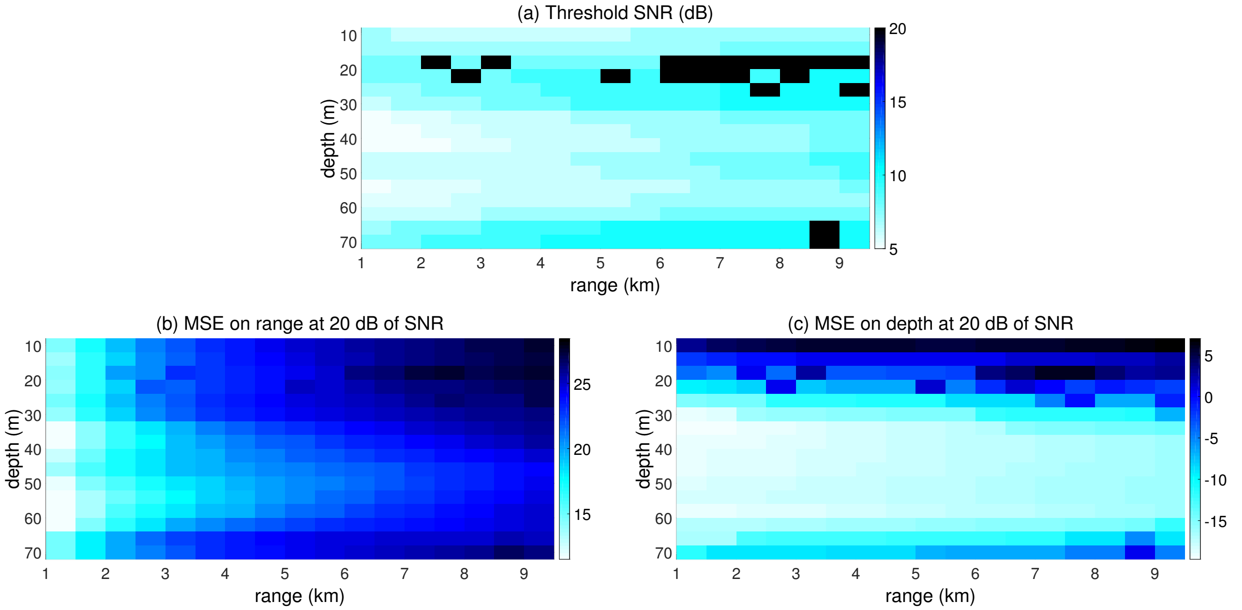

Fig. 9. Inversion using environment B. (a) Threshold SNR, (b) range MSE with SNR=20 dB, (c) depth MSE with SNR=20 dB. Every subfigure is computed over the search space $r_s \in [500, 10000]$ m and $z_s \in [5, 75]$ m. Receiver depth is $z_r = 20$ m. Seabed sound speed is $c_{bb} = 1625$ m/s.

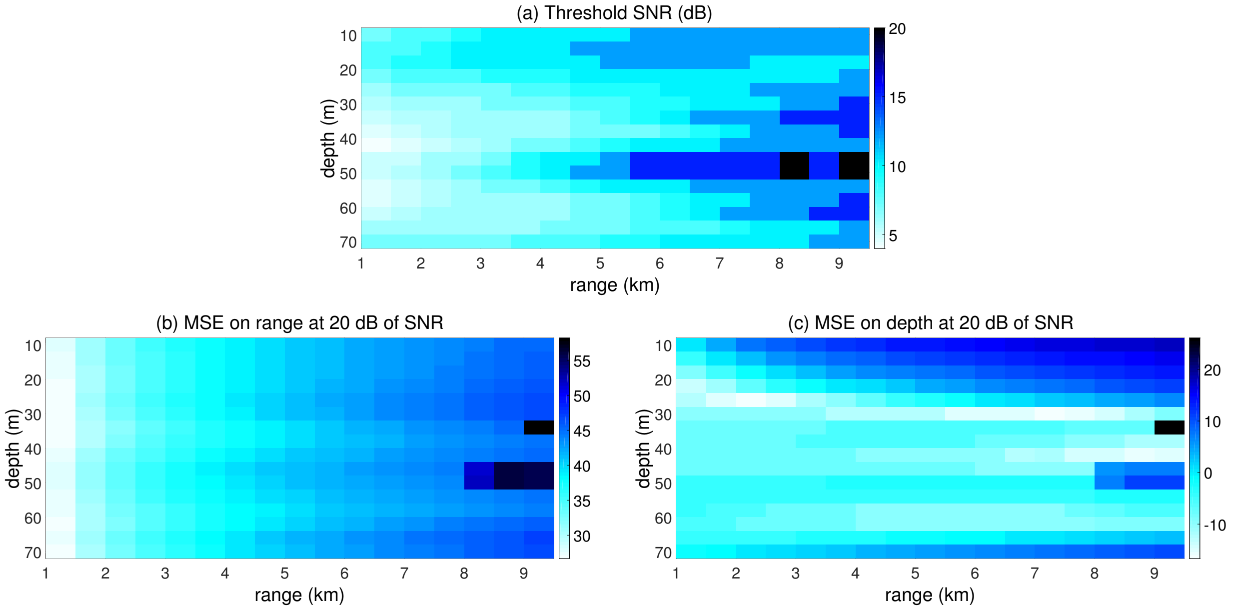

Fig. 10. Inversion using environment B. (a) Threshold SNR, (b) range MSE with SNR=20 dB, (c) depth MSE with SNR=20 dB. Every subfigure is computed over the search space $r_s \in [500, 10000]$ m and $z_s \in [5, 75]$ m. Receiver depth is $z_r = 20$ m. Seabed sound speed is $c_{bb} = 1675$ m/s.

2) Inversion using environment C: The environment C is representative of a significant lack of knowledge of both the seabed and water column properties. Fig. 11 shows the global MSE for several seabed sound speed values c_{bc} (in environment C). A striking feature is that the performance is strongly impacted by the mismatch. The RMSE is never smaller than 696 m in range (MSE=56.85 dB) and never smaller than 13 m in depth (MSE=22.32 dB). The performance depends on the c_{bc} values, but there does not seem to have a physical link between the performance and the c_{bc} value. None of the c_{bc} values allow approximating the propagation in environment A using environment C.

Fig. 12 shows the SNR threshold, the range MSE at 20 dB and the depth MSE at 20 dB in the (z_s, r_s) domain for a seabed speed $c_{bb} = 1600$ m/s. The SNR threshold variations do not seem to follow a particular pattern. The range MSE increases with source range but does not vary much with source depth. The depth MSE is particularly high in several regions. Because the difference between environment A and C is large, it is difficult to make physical links between the mismatch and the performance (apart from the trivial remark that the MSE is larger when both the water column and seabed are unknown).

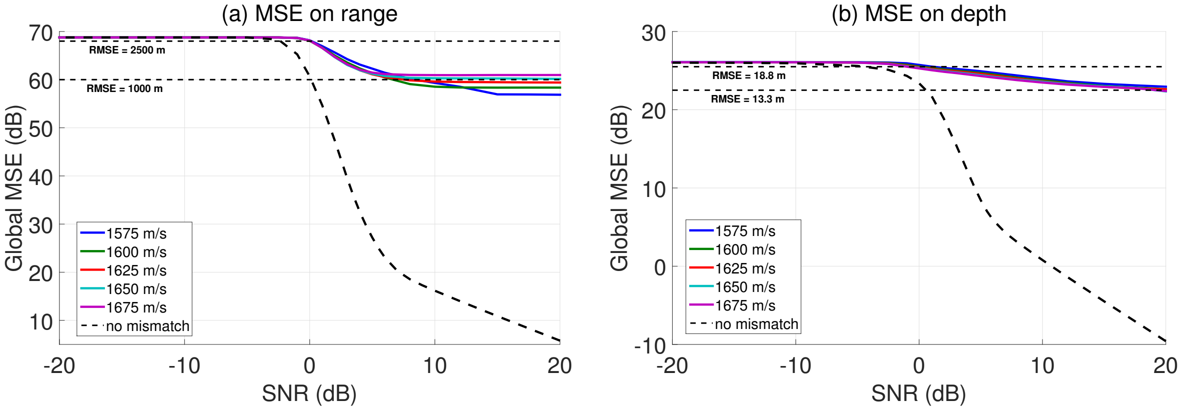

Fig. 11. Inversion using environment C. Global MSE over $r_s \in [500, 10000]$ m and $z_s \in [5, 75]$ m for several seabed sound speeds c_{bc}. Receiver depth is $z_r = 20$ m.

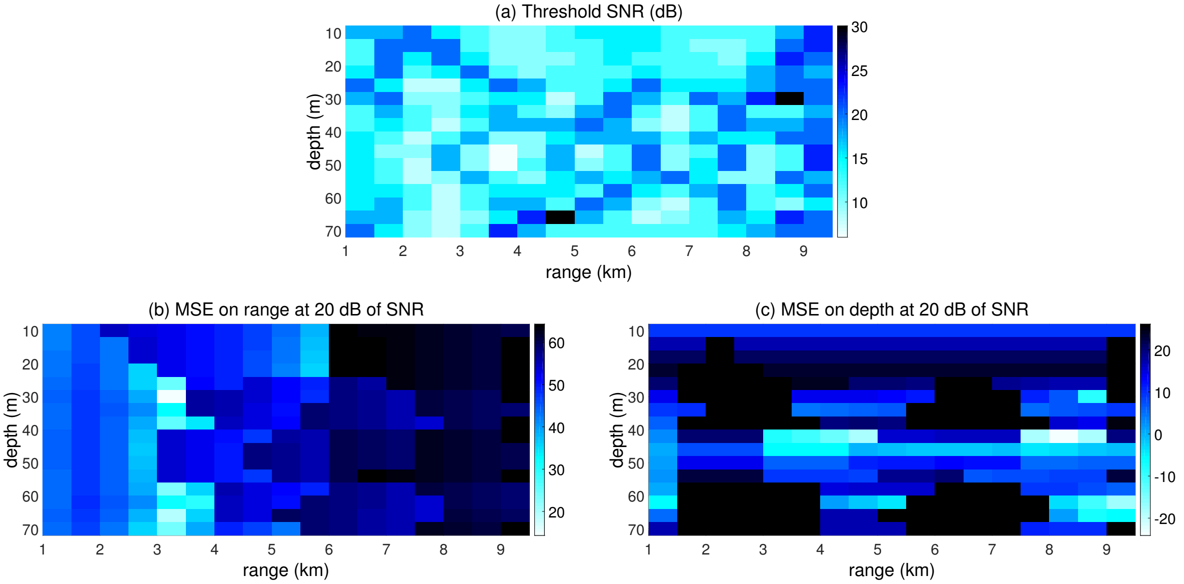

Fig. 12. Inversion using environment C. (a) Threshold SNR, (b) range MSE with SNR=30 dB, (c) depth MSE with SNR=30 dB. Every subfigure is computed over the search space $r_s \in [500, 10000]$ m and $z_s \in [5, 75]$ m. Receiver depth is $z_r = 20$ m. Seabed sound speed is $c_{bc} = 1600$ m/s.

F. Impact of mode filtering

In this section, the impact of non-ideal mode filtering is evaluated by considering degradations resulting from mode filtering as mismatch. Formally, we first simulate the time domain signal that contains all the propagating modes. We then apply modal filtering using warping (see Sec. II-A) to obtain the extracted modes $\mathbf{x}(f_k, \boldsymbol{\theta})$ and evaluate the performance when using the mode replicas $\mathbf{x}_\epsilon(f_k, \boldsymbol{\theta})$ to carry inversion with or without environmental mismatch. Because of the tedious non-automatic task of modal filtering, the results presented here only correspond to a single source position $(z_s, r_s) = (40\text{ m}, 5000\text{ m})$.

1) Inversion without environmental mismatch: The results when there is no environmental mismatch are presented in Fig. 13. It can be seen that modal filtering has a moderate effect on the performance. The SNR threshold is around 5 dB without or with modal filtering mismatch and the asymptotic error stays small (around 5 m in range and 30 cm in depth). As a reminder, the results presented in Fig. 13 are valid for a single source position $(z_s, r_s) = (40\text{ m}, 5000\text{ m})$. Performance may vary for other source positions.

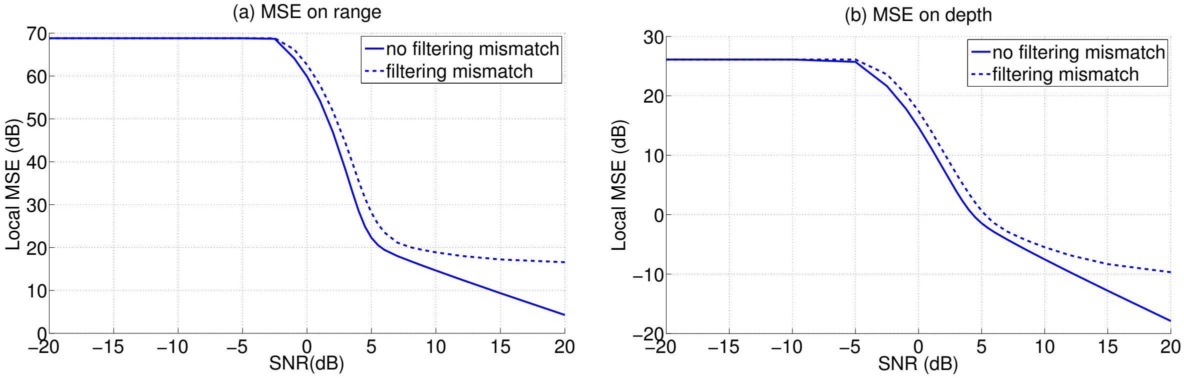

Fig. 13. No environmental mismatch. SR-MMP performance without and with modal filtering mismatch at $(z_s, r_s) = (40\ m,\ 5000\ m)$. Receiver depth is $z_r = 20$ m.

2) Inversion with environmental mismatch (environment B and C): The results when there no environmental mismatch are presented in Fig. 14 for environment B and in Fig. 15 for environment C. Again, it can be seen that modal filtering has a moderate effect on the performance as the curves without filtering mismatch (solid lines) and the curves with filtering mismatch (dashed lines) are generally close. Sometimes, the performance is even a little bit better with filtering mismatch. A possible explanation is that modal filtering sometimes removes (or attenuates) the parts of modes that are the most affected by the seabed properties.

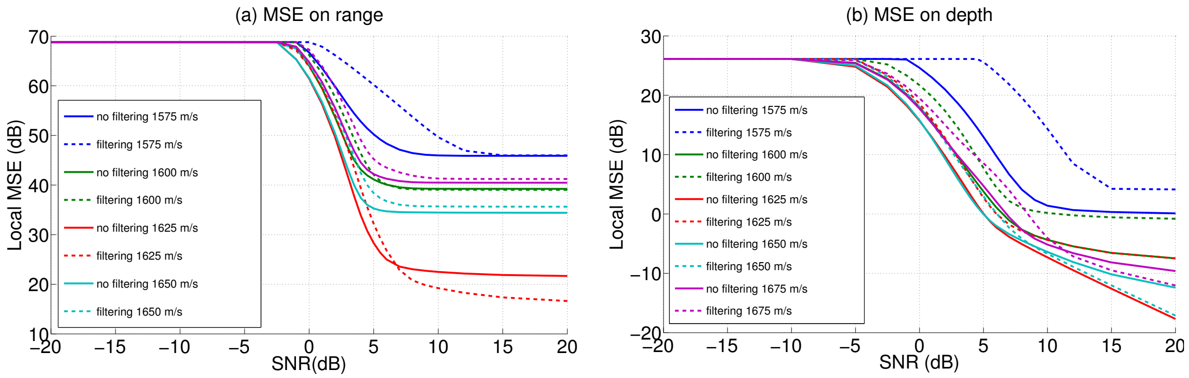

Fig. 14. Environmental mismatch B. SR-MMP performance without and with modal filtering mismatch at $(z_s, r_s) = (40\ m,\ 5000\ m)$. Receiver depth is $z_r = 20$ m.

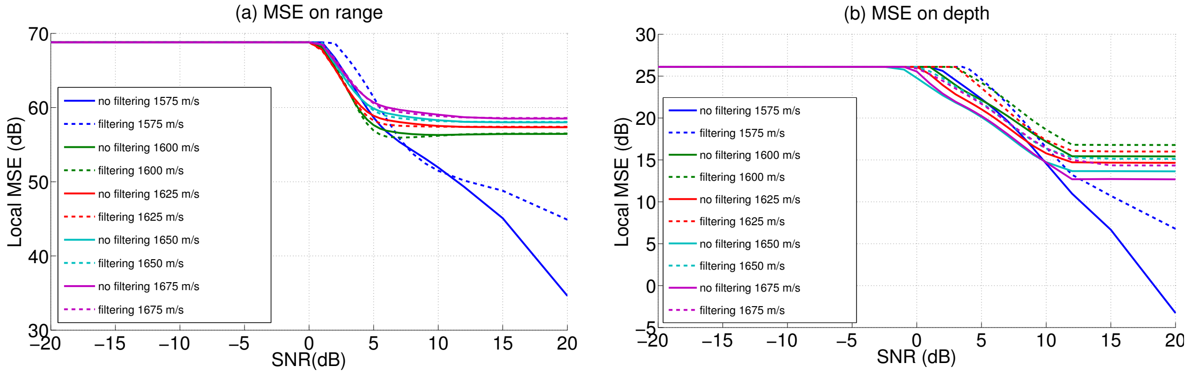

Fig. 15. Environmental mismatch C. SR-MMP performance without and with modal filtering mismatch and environmental mismatch at $(z_s, r_s) = (40\ m,\ 5000\ m)$. Receiver depth is $z_r = 20$ m.

V. CONCLUSIONS

Single receiver matched-mode processing performances have been evaluated in typical source localization scenarios. The SR-MMP ambiguity function exhibits a mainlobe/sidelobe behavior characteristic of non-linear estimation problems, and the mean-square error presents three regions of operation as a function of SNR: the high SNR asymptotic region driven by mainlobe errors, the intermediate SNR threshold region driven by sidelobe errors and the low SNR no-information region. The method of interval errors, which gives approximate but computationally efficient and reliable MSE performance prediction, has been used to conduct multiple performance analyses. The performances have first been analyzed when there is no mismatch between the assumed environment and the true environment. SR-MMP performances highly depend on the source/receiver depth. In particular, a significant loss in performance is observed when the receiver is located at a node common to two modes which shows that receiver depth must be chosen with care. In the example studied here, an SNR of 3 dB seemed enough to obtain acceptable performance, although this number may vary significantly in other cases (different environment, frequencies or number of modes).

When there is mismatch between the assumed and true seabed (bottom halfspace assumed instead of two layer bottom over bottom halfspace) performance deteriorates, the threshold region begins at higher SNR and there is a bias at high SNR. However, it seems to remain acceptable as long as the chosen bottom sound speed is not too far from the true bottom layers sound speeds. The results suggest that it is possible to obtain decent performances by seeking the bottom halfspace sound-speed that best approximates the real bottom. This would be an alternative to more complicated localization algorithms that jointly invert over source locations and environmental parameters (e.g. [41]). When there is mismatch in both the seabed and the water sound speed profile (constant sound speed profile instead of a thermocline), there is a significant loss in performance. It appears that in this case, the difference between the assumed environment and the true environment is too strong to obtain acceptable performance. Furthermore, the impact of possible degradations resulting from non-ideal modal filtering has also been investigated: modal filtering seems to only have a moderate impact on performance.

The analysis presented here provides a better understanding of SR-MMP and its achievable performance. It therefore offers good prospects for future application of SR-MMP. Furthermore, while the influence of mismatch on performances have been analyzed, another prospect could be to develop methods for improving the robustness of SR-MMP to environmental mismatch. A possible approach would be to adapt ideas implemented for MFP [42]–[44].

VI. ACKNOWLEDGEMENT

This work was funded by the French Government Defence procurement agency (Direction Générale de l'Armement). JB also acknowledges the Investment in Science Fund at WHOI.

APPENDIX A

PAIRWISE ERROR PROBABILITY

The pairwise error probability $P_e(\boldsymbol{\theta}_n|\boldsymbol{\theta}_\mathrm{m})$ of the ML estimator (under a possible model mismatch) is given by

$$P_e(\boldsymbol{\theta}_n|\boldsymbol{\theta}_\mathrm{m}) = \mathbb{P}\left(\sum_{k=1}^{K} \frac{|\bar{\mathbf{x}}_\epsilon^H(f_k,\boldsymbol{\theta}_n)\mathbf{y}(f_k)|^2 - |\bar{\mathbf{x}}_\epsilon^H(f_k,\boldsymbol{\theta}_\mathrm{m})\mathbf{y}(f_k)|^2}{\sigma_\mathbf{w}^2(f_k)} \geq 0\right). \tag{13}$$

Following the same approach as in [33, Sec. III-A], this pairwise error probability can be expressed as

$$P_e(\boldsymbol{\theta}_n|\boldsymbol{\theta}_{\mathrm{m}}) = 1 - \frac{1}{2\pi}\int_{-\infty}^{\infty}\frac{1}{j\omega+\beta}\times\frac{e^{-c}}{\prod_{k=1}^{K}(1+\lambda_{1_k}(j\omega+\beta))(1+\lambda_{2_k}(j\omega+\beta))}d\omega, \tag{14}$$

$$c = \sum_{k=1}^{K}\frac{\lambda_{1_k}|\mu_{1_k}|^2(j\omega+\beta)}{(1+\lambda_{1_k}(j\omega+\beta))} + \frac{\lambda_{2_k}|\mu_{2_k}|^2(j\omega+\beta)}{(1+\lambda_{2_k}(j\omega+\beta))}, \tag{15}$$

for some $\beta > 0$ such that $1+\beta\lambda_{1_k} > 0$ and $1+\beta\lambda_{2_k} > 0$. $\lambda_{1_k,2_k}$ are the non-zero eigenvalues of

$$\overline{\mathbf{x}}_\epsilon(f_k,\boldsymbol{\theta}_n)\overline{\mathbf{x}}_\epsilon{}^H(f_k,\boldsymbol{\theta}_n) - \overline{\mathbf{x}}_\epsilon(f_k,\boldsymbol{\theta}_{\mathrm{m}})\overline{\mathbf{x}}_\epsilon{}^H(f_k,\boldsymbol{\theta}_{\mathrm{m}}) \tag{16}$$

and satisfy

$$\lambda_{1_k,2_k} = \pm\sqrt{1 - |\overline{\mathbf{x}}_\epsilon{}^H(f_k,\boldsymbol{\theta}_n)\overline{\mathbf{x}}_\epsilon(f_k,\boldsymbol{\theta}_{\mathrm{m}})|}. \tag{17}$$

The values $\mu_{1_k},\ \mu_{2_k}$ can be expressed as a function of the SNR $\gamma(f_k)$. In the general case with possible mismatch they satisfy

$$\mu_{1_k,2_k} = \sqrt{\frac{\gamma(f_k)(1-\lambda_{1_k,2_k})}{2\lambda^2_{1_k,2_k}}}\times\Bigg(\overline{\mathbf{x}}_\epsilon{}^H(f_k,\boldsymbol{\theta}_{\mathrm{m}})\overline{\mathbf{x}}(f_k,\boldsymbol{\theta}_0) - \frac{1}{1-\lambda_{1_k,2_k}}\times$$
$$\overline{\mathbf{x}}_\epsilon{}^H(f_k,\boldsymbol{\theta}_{\mathrm{m}})\overline{\mathbf{x}}_\epsilon(f_k,\boldsymbol{\theta}_n)\overline{\mathbf{x}}_\epsilon{}^H(f_k,\boldsymbol{\theta}_n)\overline{\mathbf{x}}(f_k,\boldsymbol{\theta}_0)\Bigg). \tag{18}$$

APPENDIX B

ASYMPTOTIC MSE

When expanded, the MSE can be expressed as

$$\mathbb{E}_{\mathbf{y}}\left\{\left(\hat{\boldsymbol{\theta}}-\boldsymbol{\theta}_0\right)\left(\hat{\boldsymbol{\theta}}-\boldsymbol{\theta}_0\right)^T\right\} = \mathbb{E}_{\mathbf{y}}\left\{\Delta\hat{\boldsymbol{\theta}}\Delta\hat{\boldsymbol{\theta}}^T\right\} + \mathbb{E}_{\mathbf{y}}\left\{\Delta\hat{\boldsymbol{\theta}}\right\}\mathbf{b}^T(\boldsymbol{\theta}_0) + \mathbf{b}(\boldsymbol{\theta}_0)\mathbb{E}_{\mathbf{y}}\left\{\Delta\hat{\boldsymbol{\theta}}\right\}^T + \mathbf{b}(\boldsymbol{\theta}_0)\mathbf{b}^T(\boldsymbol{\theta}_0), \tag{19}$$

where $\Delta\hat{\boldsymbol{\theta}} = \hat{\boldsymbol{\theta}} - \boldsymbol{\theta}_{\mathrm{m}}$ and $\mathbf{b}(\boldsymbol{\theta}_0) = \boldsymbol{\theta}_{\mathrm{m}} - \boldsymbol{\theta}_0$. The value $\boldsymbol{\theta}_{\mathrm{m}}$ as well as the bias $\mathbf{b}(\boldsymbol{\theta}_0)$ can easily be obtained by analyzing the AF. The asymptotic local MSE is then derived by computing an asymptotic approximation of $\mathbb{E}_{\mathbf{y}}\left\{\Delta\hat{\boldsymbol{\theta}}\Delta\hat{\boldsymbol{\theta}}^T\right\}$ and $\mathbb{E}_{\mathbf{y}}\left\{\Delta\hat{\boldsymbol{\theta}}\right\}$. Based on [33, Sec. III-B], we obtain the following results. Define

$$\mathbf{a}_k = \overline{\mathbf{x}}_\epsilon(f_k,\boldsymbol{\theta}_{\mathrm{m}}),\ \mathbf{c}_k = \mathbf{x}(f_k,\boldsymbol{\theta}_0),\ \mathbf{D}_k = \frac{\partial\overline{\mathbf{x}}_\epsilon(f_k,\boldsymbol{\theta}_{\mathrm{m}})}{\partial\boldsymbol{\theta}^T}, \tag{20}$$

and the $M \times M$ matrix

$$[\mathbf{F}]_{i,j} = \sum_{k=1}^{K}\frac{|s(f_k)|^2}{\sigma^2_{\mathbf{w}}(f_k)}\mathrm{Re}\Bigg[\left(\frac{\partial^2\mathbf{a}_k}{\partial\theta_j\partial\theta_i}\right)^H\mathbf{c}_k\mathbf{c}_k^H\mathbf{a}_k + \left(\frac{\partial\mathbf{a}_k}{\partial\theta_i}\right)^H\mathbf{c}_k\mathbf{c}_k^H\left(\frac{\partial\mathbf{a}_k}{\partial\theta_j}\right)\Bigg]. \tag{21}$$

We then obtain

$$\mathbb{E}_{\mathbf{y}}\left\{\Delta\hat{\boldsymbol{\theta}}\right\} = -\mathbf{F}^{-1}\mathrm{Re}\left[\sum_{k=1}^{K}\mathbf{D}_k^H\mathbf{a}_k\right], \tag{22}$$

and

$$\begin{aligned}\mathbb{E}_{\mathbf{y}}\left\{\Delta\hat{\boldsymbol{\theta}}\Delta\hat{\boldsymbol{\theta}}^T\right\} &= \frac{1}{2}\mathbf{F}^{-1}\mathrm{Re}\Bigg[\sum_{k=1}^{K}\left(\mathbf{D}_k^H\mathbf{D}_k + \mathbf{D}_k^H\mathbf{a}_k\mathbf{a}_k^T\mathbf{D}_k^*\right)\\ &+ \frac{|s(f_k)|^2}{\sigma_{\mathbf{w}}^2(f_k)}\left(\mathbf{D}_k^H\mathbf{c}_k\mathbf{c}_k^H\mathbf{D}_k + \mathbf{D}_k^H\mathbf{c}_k\mathbf{c}_k^H\mathbf{a}_k\mathbf{a}_k^T\mathbf{D}_k^* + \mathbf{D}_k^H\mathbf{D}_k\mathbf{a}_k^H\mathbf{c}_k\mathbf{c}_k^H\mathbf{a}_k + \mathbf{D}_k^H\mathbf{a}_k\mathbf{c}_k^T\mathbf{D}_k^*\mathbf{c}_k^H\mathbf{a}_k\right)\Bigg]\mathbf{F}^{-1}\\ &+ \mathbb{E}_{\mathbf{y}}\left\{\Delta\hat{\boldsymbol{\theta}}\right\}\mathbb{E}_{\mathbf{y}}\left\{\Delta\hat{\boldsymbol{\theta}}\right\}^T.\end{aligned} \tag{23}$$

REFERENCES

[1] A.B. Baggeroer, W.A. Kuperman, and P.N. Mikhalevsky, "An overview of matched field methods in ocean acoustics," *IEEE Journal of Oceanic Engineering*, vol. 18, no. 4, pp. 401–424, 1993.

[2] F.B. Jensen, W.A. Kuperman, and B. Michael, *Computational ocean acoustics*, American Institute of Physics, New York, 1994.

[3] R.G. Baraniuk and D.L. Jones, "Unitary equivalence: A new twist on signal processing," *IEEE Transactions on Signal Processing*, vol. 43, no. 10, pp. 2269–2282, 1995.

[4] G. Le Touzé, B. Nicolas, J. Mars, and J.L. Lacoume, "Matched representations and filters for guided waves," *IEEE Transactions on Signal Processing*, vol. 57, no. 5, pp. 1783–1795, 2009.

[5] J. Bonnel, C. Gervaise, P. Roux, B. Nicolas, and JI Mars, "Modal depth function estimation using time-frequency analysis," *The Journal of the Acoustical Society of America*, vol. 130, pp. 61–71, 2011.

[6] J. Bonnel, G. Le Touzé, B. Nicolas, and J. Mars, "Physics-based time-frequency representations for underwater acoustics: Power class utilization with waveguide-invariant approximation," *IEEE Signal Processing Magazine*, vol. 30, no. 6, pp. 120–129, 2013.

[7] J. Bonnel, A. M. Thode, S. B. Blackwell, K. Kim, and A M. Macrander, "Range estimation of bowhead whale (balaena mysticetus) calls in the arctic using a single hydrophonea," *The Journal of the Acoustical Society of America*, vol. 136, no. 1, pp. 145–155, 2014.

[8] A. Thode, J. Bonnel, M. Thieury, A. Fagan, C. Verlinden, D. Wright, C. Berchok, and J. Crance, "Using nonlinear time warping to estimate north pacific right whale calling depths in the bering sea," *The Journal of the Acoustical Society of America*, vol. 141, no. 5, pp. 3059–3069, 2017.

[9] G.R. Wilson, R.A. Koch, and P.J. Vidmar, "Matched mode localization," *The Journal of the Acoustical Society of America*, vol. 84, no. 1, pp. 310–320, 1988.

[10] T.C. Yang, "Effectiveness of mode filtering: A comparison of matched-field and matched-mode processing," *The Journal of the Acoustical Society of America*, vol. 87, no. 5, pp. 2072–2084, 1990.

[11] C.W. Bogart and T.C. Yang, "Comparative performance of matched-mode and matched-field localization in a range-dependent environment," *The Journal of the Acoustical Society of America*, vol. 92, pp. 2051, 1992.

[12] N.E. Collison and S.E. Dosso, "Regularized matched-mode processing," *The Journal of the Acoustical Society of America*, vol. 103, pp. 2821, 1998.

[13] T.B. Neilsen and E.K. Westwood, “Extraction of acoustic normal mode depth functions using vertical line array data,” *The Journal of the Acoustical Society of America*, vol. 111, pp. 748–756, 2002.

[14] K. Yoo and T.C. Yang, “Broadband source localization in shallow water in the presence of internal waves,” *The journal of the Acoustical Society of America*, vol. 106, no. 6, pp. 3255–3269, 1999.

[15] G. R Potty, J. H Miller, J. F Lynch, and K. B Smith, “Tomographic inversion for sediment parameters in shallow water,” *The Journal of the Acoustical Society of America*, vol. 108, no. 3, pp. 973–986, 2000.

[16] S.D. Rajan and K.M. Becker, “Inversion for range-dependent sediment compressional-wave-speed profiles from modal dispersion data,” *IEEE Journal of Oceanic Engineering*, vol. 35, no. 1, pp. 43–58, 2010.

[17] J. Bonnel, S. E Dosso, and N R. Chapman, “Bayesian geoacoustic inversion of single hydrophone light bulb data using warping dispersion analysis,” *The Journal of the Acoustical Society of America*, vol. 134, no. 1, pp. 120–130, 2013.

[18] L. Wan, J.X. Zhou, and P.H. Rogers, “Low-frequency sound speed and attenuation in sandy seabottom from long-range broadband acoustic measurements,” *The Journal of the Acoustical Society of America*, vol. 128, no. 2, pp. 578–589, 2010.

[19] J. Zeng, N R. Chapman, and J. Bonnel, “Inversion of seabed attenuation using time-warping of close range data,” *The Journal of the Acoustical Society of America*, vol. 134, no. 5, pp. EL394–EL399, 2013.

[20] G. Le Touzé, J. Torras, B. Nicolas, and Jérôme Mars, “Source localization on a single hydrophone,” in *OCEANS*. IEEE, 2008, pp. 1–6.

[21] G. Le Touzé, *Localisation de source par petits fonds en UBF (1-100 Hz) à l’aide d’outils temps-fréquence*, Ph.D. thesis, Institut National Polytechnique de Grenoble, 2007.

[22] B. Nicolas, G. Le Touzé, C. Soares, S. Jesus, and JI Marsal, “Incoherent versus coherent matched mode processing for shallow water source localisation using a single hydrophone,” *Instrumentation viewpoint*, vol. 8, pp. 67–68, 2009.

[23] J. Bonnel and A. Thode, “Range and depth estimation of bowhead whale calls in the arctic using a single hydrophone,” in *Sensor Systems for a Changing Ocean (SSCO)*. IEEE, 2014, pp. 1–4.

[24] Harry L Van Trees, *Detection, Estimation, and Linear Modulation Theory, Part I*, Wiley, New York, 1968.

[25] C.D. Richmond, “Mean-squared error and threshold snr prediction of maximum-likelihood signal parameter estimation with estimated colored noise covariances,” *IEEE Transactions on Information Theory*, vol. 52, no. 5, pp. 2146–2164, 2006.

[26] A.B. Baggeroer and H. Schmidt, “Cramer-rao bounds for matched field tomography and ocean acoustic tomography,” in *International Conference on Acoustics, Speech and Signal Processing (ICASSP)*. IEEE, 1995, vol. 5, pp. 2763–2766.

[27] J. Tabrikian and J.L. Krolik, “Barankin bounds for source localization in an uncertain ocean environment,” *IEEE Transactions on Signal Processing*, vol. 47, no. 11, pp. 2917–2927, 1999.

[28] W. Xu, A.B. Baggeroer, and C.D. Richmond, “Bayesian bounds for matched-field parameter estimation,” *IEEE Transactions on Signal Processing*, vol. 52, no. 12, pp. 3293–3305, 2004.

[29] Wen Xu, Arthur B Baggeroer, and Henrik Schmidt, “Performance analysis for matched-field source localization: Simulations and experimental results,” *IEEE Journal of Oceanic Engineering*, vol. 31, no. 2, pp. 325–344, 2006.

[30] W. Xu, Z. Xiao, and L. Yu, “Performance analysis of matched-field source localization under spatially correlated noise field,” *IEEE Journal of Oceanic Engineering*, vol. 36, no. 2, pp. 273–284, 2011.

[31] Y. Le Gall, F.-X. Socheleau, and J. Bonnel, “Performance analysis of single receiver matched-mode processing for source localization,” in *2nd Underwater Acoustics Conference and Exhibition (UA2014)*, 2014.

[32] Y. Le Gall, F.-X. Socheleau, and J. Bonnel, “Matched-Field Processing Performance Under the Stochastic and Deterministic Signal Models,” *IEEE Transactions on Signal Processing*, vol. 62, no. 22, pp. 5825–5838, 2014.

[33] Y. Le Gall, F.-X. Socheleau, and J. Bonnel, "Matched-Field Performance Prediction with Model Mismatch," *IEEE Signal Processing Letters*, vol. 23, no. 4, pp. 409 – 413, 2016.

[34] C.F. Mecklenbräuker and P. Gerstoft, "Objective functions for ocean acoustic inversion derived by likelihood methods," *Journal of Computational Acoustics*, vol. 8, no. 02, pp. 259–270, 2000.

[35] S. E Dosso and M. J. Wilmut, "Maximum-likelihood and other processors for incoherent and coherent matched-field localization," *The Journal of the Acoustical Society of America*, vol. 132, no. 4, pp. 2273–2285, 2012.

[36] Y. Pawitan, *In all likelihood: statistical modelling and inference using likelihood*, Oxford University Press, 2001.

[37] H.L. Van Trees and K.L. Bell, *Bayesian bounds for parameter estimation and nonlinear filtering/tracking*, Wiley-IEEE Press, 2007.

[38] C. D. Richmond, "Capon algorithm mean-squared error threshold snr prediction and probability of resolution," *IEEE Transactions on Signal Processing*, vol. 53, no. 8, pp. 2748–2764, 2005.

[39] C. D. Richmond, "On the threshold region mean-squared error performance of maximum-likelihood direction-of arrival estimation in the presence of signal model mismatch," in *Workshop on Sensor Array and Multichannel Processing*. IEEE, 2006, pp. 268–272.

[40] F. Athley, "Threshold region performance of maximum likelihood direction of arrival estimators," *IEEE Transactions on Signal Processing*, vol. 53, no. 4, pp. 1359–1373, 2005.

[41] S. E. Dosso and M. J. Wilmut, "Comparison of focalization and marginalization for bayesian tracking in an uncertain ocean environment," *The Journal of the Acoustical Society of America*, vol. 125, no. 2, pp. 717–722, 2009.

[42] J.L. Krolik, "Matched-field minimum variance beamforming in a random ocean channel," *The Journal of the Acoustical Society of America*, vol. 92, no. 3, pp. 1408–1419, 1992.

[43] J. Tabrikian, J.L. Krolik, and H. Messer, "Robust maximum-likelihood source localization in an uncertain shallow-water waveguide," *The Journal of the Acoustical Society of America*, vol. 101, no. 1, pp. 241–249, 1997.

[44] Y. Le Gall, S. E Dosso, F.-X. Socheleau, and J. Bonnel, "Bayesian source localization with uncertain green's function in an uncertain shallow water ocean," *The Journal of the Acoustical Society of America*, vol. 139, no. 3, pp. 993 – 1004, 2016.

PLACE
PHOTO
HERE

Yann Le Gall (S'12) received the Dipl.Ing. degree in signal processing from Grenoble Institut National Polytechnique (Grenoble INP), Grenoble, France, in 2012, and the Ph.D. degree in signal processing at Lab-STICC (UMR 6285), ENSTA Bretagne, Brest, France in 2015. He is currently a research engineer at Thales Underwater Systems, Brest, France. His research interests in the field of signal processing and underwater acoustics include source detection/localization, geoacoustic inversion and performance prediction.

PLACE
PHOTO
HERE

Francois-Xavier Socheleau (S'08-M'12) graduated in electrical engineering from ESEO, Angers, France, in 2001 and received the Ph.D. degree from Telecom Bretagne, Brest, France, in 2011.

From 2001 to 2004, he was a Research Engineer at Thales Communications, France, where he worked on electronic warfare systems. From 2005 to 2007, he was employed at Navman Wireless (New Zealand/U.K.) as an R&D Engineer. From 2008 to 2011, he worked for Thales Underwater Systems, France. In November 2011, he joined ENSTA Bretagne as an Assistant Professor. Since September 2014, he has been an Associate Professor at IMT Atlantique (formerly known as Telecom Bretagne), France. His research interests include signal processing, wireless communications and underwater acoustics.

PLACE
PHOTO
HERE

Julien Bonnel (S'08 - M'11) received the Ph.D. degree in signal processing from Grenoble Institut National Polytechnique (Grenoble INP), Grenoble, France, in 2010.

From 2010 to 2017, he was an Assistant Professor at Lab-STICC (UMR 6285), ENSTA Bretagne in Brest, France. Since September 2017, he has been an Associate Scientist at Woods Hole Oceanographic Institution, USA. His research in signal processing and underwater acoustics include time-frequency analysis, source detection/localization, geoacoustic inversion, acoustical tomography, passive acoustic monitoring, and bioacoustics. He is a Member of the Acoustical Society of America.